

## Mid-infrared images and models of the $\beta$ Pictoris dust disk<sup>\*</sup>

E. Pantin<sup>1</sup>, P.O. Lagage<sup>2</sup>, and P. Artymowicz<sup>3</sup>

<sup>1</sup> CEA/DSM/DAPNIA Service d'Astrophysique F-91191 Gif-sur-Yvette Cedex and Jussieu University, 5 place Jussieu, F-75005 Paris, France

<sup>2</sup> CEA/DSM/DAPNIA Service d'Astrophysique (URA 2052 associée au CNRS) F-91191 Gif-sur-Yvette Cedex, France

<sup>3</sup> Stockholm Observatory, Stockholm University, S-133 36 Saltjöbaden, Sweden

Received 14 August 1996 / Accepted 31 January 1997

**Abstract.** New high resolution mid-infrared images of the inner part of the  $\beta$  Pictoris circumstellar dust disk are reported. These data are used to probe the inner disk geometry and to derive the 0-100 AU radial density profile, with a spatial resolution of 5 AU. Realistic grains (porous silicates with a core of olivine and pyroxene coated with a mantle “organic refractories”) rather than solid Draine and Lee silicates, have been incorporated in models describing the dust thermal emission. In a first set of models, we assume a single composition for the grains. These models are not able to fully reproduce simultaneously our data and the IRAS fluxes. In a second set of models, we introduce another component, consisting of particles containing some ice beyond a limit around 90-100 AU. Such a model fulfils all the observational constraints (including the visible scattered flux) and resolves the discrepancy concerning the particles albedo which is predicted to be too small in the first set of models. It also predicts an ice feature at 50  $\mu\text{m}$ ; a feature around 6  $\mu\text{m}$  characteristic of the organic refractory material; and several crystalline olivine features at 24, 28 and 35  $\mu\text{m}$ . These features should be observable with the Short Wavelength Spectrometer (SWS) and Long Wavelength Spectrometer (LWS) on board the Infrared Space Observatory. 20  $\mu\text{m}$  images should also show an abrupt cut-off around 90-100 AU due to the change of the grains composition. ISOCAM should image essentially the scattered starlight, showing the transition between the thermal emission of the inner, non-icy, component, and the scattered emission in the mid-infrared range from the outer component containing ice.

**Key words:** stars individual:  $\beta$  Pictoris – dust – stars: infrared – planetary systems

### 1. Introduction

At a distance of 16.5 pc from the Earth lies the star  $\beta$  Pictoris for which the infrared excess detected by IRAS (Aumann 1984) was attributed to a dusty disk in an intermediate stage between the solar protoplanetary nebulae and an actual solar system (e.g.

review by Artymowicz, 1994 and references therein). This system was studied from the UV (Deleuil et al., 1993 and references therein) to the millimeter range (Chini et al., 1991). Circumstellar dust grains producing the infrared excess are present with sizes ranging from the  $\mu\text{m}$  domain to the mm domain (e.g. see the review by Artymowicz (1994) and references therein) and are arranged geometrically in a disk seen almost edge-on (Smith and Terrile, 1984). A gaseous component is also present around the star (Sletteback and Carpenter, 1983; review by Vidal-Madjar and Ferlet, 1994 and references therein). Sporadic gas pockets, revealed by UV and visible spectroscopic observations of redshifted metallic lines seen in absorption (Kondo and Bruhweiler, 1985; Ferlet, Hobbs and Vidal-Madjar, 1987; Lagrange, Ferlet and Vidal-Madjar, 1987), are attributed to the evaporation of kilometer sized bodies, perhaps the  $\beta$  Pic analogue of comets, as they fall onto the star (Beust, 1994 and references therein). Slow evaporation of a belt of bodies orbiting at 15-30 AU from the star (somewhat analogous to the Kuiper belt) is also the main ingredient for a model recently proposed to explain the spatial profile of the outer part of the dusty disk (Lecavelier des Etangs et al., 1995).

The study of the inner part of the dusty disk ( $r < 100$  AU) is very exciting since it is where planets could exist. In visible, ground-based observations, the contrast between the star and the disk is so high that blooming (charge leakage) and seeing effects have made it impossible to observe the disk within 30 AU from the central star (Golimovski et al., 1993; Lecavelier des Etangs et al., 1993; Kalas and Jewitt, 1995). Even the recent HST observations did not give access to the region within 20 AU (Burrows et al., 1995). A similar limit is reached with ground-based near-IR observations (K band) using adaptative optics (Mouillet and Lagrange, 1996). As shown by Lagage and Pantin (1994, hereafter LP94), the inner region is accessible to mid-IR observations. The first images have shown an inner region deficient in matter, as expected by the models developed to fit the IRAS spectral energy distribution (Gillett, 1986; Diner and Appleby, 1986; Telesco, Becklin and Wolstencroft, 1986; Artymowicz, Burrows and Paresce, 1989; Backmann, Gillett and Witteborn, 1992), and, surprisingly, a large asymmetry between the NE and SW components of the disk.

Send offprint requests to: P.O.Lagage

<sup>\*</sup> based on data obtained at ESO 3.6m telescope, La Silla, Chile.

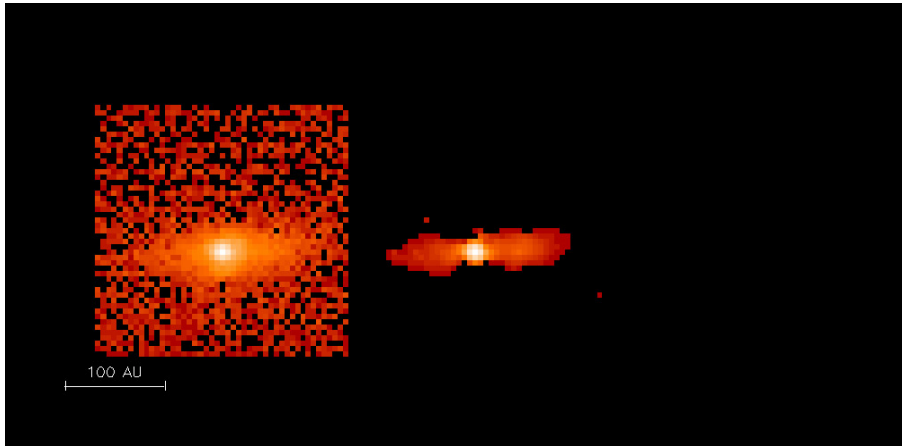


**Fig. 1.** TIMMI images of the  $\beta$  Pictoris dust disk at  $11.9 \mu\text{m}$ . The raw image is on the left and the image deconvolved using Multi-Scale Maximum Entropy Method is on the right. The pixel field of view is  $0.33''$ . The resolution achieved in the deconvolved image is very close to  $0.33 \text{ arcsec}$ .

In order to confirm and improve these preliminary results, we re-observed  $\beta$  Pictoris, again with the mid-infrared camera TIMMI (Thermal Infrared Multi Mode Instrument) mounted on the ESO 3.6m telescope at La Silla, Chile. The new set of images and the associated data reduction are discussed in Sect.2. Sect.3 presents the radial density profile from the data in the range 0-100 AU from the star. We discuss the model used to calculate the thermal emission of the grains, which is essential for inferring the density from the observed flux. The main ingredients of the model are discussed, as well as the simplifying assumptions. We determine dust composition and size distribution by using both constraints provided by the silicate feature observed in the mid-IR (Knacke et al., 1993, Aitken et al., 1993) and physical considerations, such as the dynamic behaviour of the smallest grains that experience radiation pressure forces. In Sect.4, we have extrapolated our inner density to outer regions on the basis of visible data, keeping the same composition of the grains (one component models) in order to be able to try to fit the other observables of the disk (IRAS fluxes, scattered flux, other infrared fluxes). We find that none of these one component models are able to fully reproduce the IRAS measurements. In Sect.5, we relax the assumption of uniform grain composition throughout the disk, by introducing porous silicate particles containing some ice beyond 90 AU. Sect. 6 is devoted to the discussion of some of the consequences of our model, such as the presence of an ice feature at 50 microns, which should be observable by ISO.

## 2. Observations, data reduction and first results

The observations were conducted at the ESO 3.6 meter telescope in Chile (La Silla) during November 1994 using the ESO mid-infrared camera TIMMI (Thermal Multi Mode Instrument) built by SAp (Service d'Astrophysique, CE Saclay) (Lagage et al. 1993).  $\beta$  Pictoris was observed during three nights with the smallest pixel scale of TIMMI,  $0.33 \text{ arcsec}$ , and with the  $10.5\text{-}13.3 \mu\text{m}$  band-pass filter. In order to benefit from the full pixel resolution, we have aligned the disk orientation with one of the axis of the detector, by rotating the telescope adaptor. The usual chopping and nodding techniques were used; the chopping and

nodding frequencies were respectively 6 and  $0.01 \text{ Hz}$ . To avoid the saturation of the detector by the huge ambient photon background, the image elementary integration time was set at  $7.7 \text{ ms}$ . The elementary images were coadded in real time during 20 chopping cycles. A total time of 300 min was spent on the source, which was always observed below 1.3 airmasses. The peak signal to noise ratio prior to any filtering is around 200. The nights were photometric; the number of counts recorded by the detectors varied by less than 1 percent from night to night. The nearby reference star  $\alpha$  Car was frequently monitored. The photometry is in full agreement with previous measurements ( $1.1 \text{ Jy}$  at  $11.9 \mu\text{m}$  for the disk plus star in a  $4 \text{ arcsec}$  beam diameter). The images were flat fielded by using sky images with a slightly different integration time. The array is quite homogeneous and the flat field corrections are always below 20 percent. The reference star  $\alpha$  Car is also used to remove the stellar contribution to the observed flux, as in LP94.

At  $12 \mu\text{m}$ , images are strongly degraded by diffraction, seeing and noise. To get the best angular resolution possible, we had to deconvolve (restore) the images. The Point Spread Function (PSF) was derived from observations of the reference star ( $\alpha$  Car). There are various methods to restore images. We have selected the new Multi-Scale Maximum Entropy Method developed by Pantin and Starck, 1996, because it proved to be slightly better in general than the other ones. In the case of the deconvolution of the  $\beta$  Pictoris dust disk at  $12 \mu\text{m}$ , the method does not really bring determinant improvements and similar results were obtained with standard deconvolution methods, like the regularized Richardson-Lucy algorithm with noise suppression using a multiresolution support (Richardson, 1972, Lucy, 1974, Murtagh et al., 1994; Starck et al., 1994) or the popular Maximum Entropy restoration (Gull et Skilling, 1984). The deconvolved image obtained here has a resolution of about  $0.33 \text{ arcsec}$  (from deconvolution experiments of two PSFs) and is in agreement with the one shown in LP94. The error bars have been derived from the error estimated on the PSF ( $\pm 5 \%$ ) and the subsequent error on the stellar subtraction. Nevertheless, one should note that the resulting error in the central part of the disk (and also the later derived dust density) does not exceed  $40 \%$ .

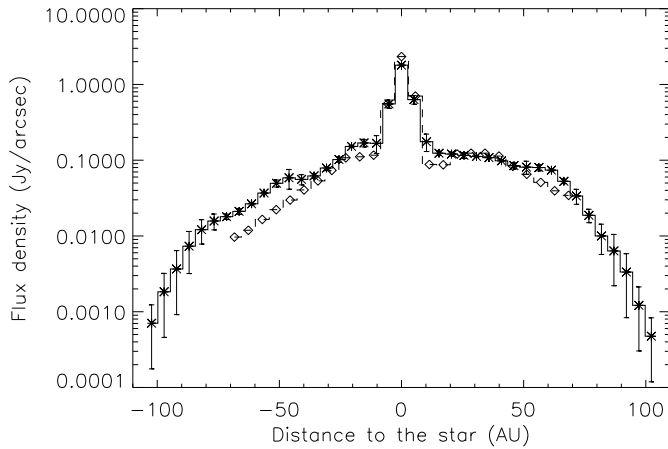


**Fig. 2.** Flux profiles obtained with the new data compared with those of LP94 (diamonds).

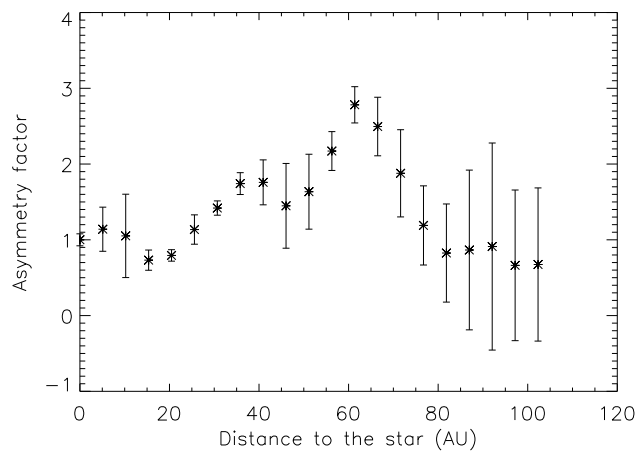


**Fig. 3.** S-W/N-E asymmetries as a function of the distance to the star

Note also that the profiles derived by LP94 and the new one are very close, when the error bars are taken into account (see Fig. 2).

The asymmetry S-W/N-E detected in LP94 is confirmed (Fig. 3), even if the new values are in the lower range of the uncertainties of the previous measurements (Pantin et al., 1995). One should note that the asymmetry is already seen in the “raw” images before deconvolution, but the very conservative errors we took concerning the deconvolution process lead to large error bars in Fig. 3. This may lead one to think that the asymmetry is only marginal, but this is not the case.

As the observations of November 94 are better than the earlier one in terms of angular resolution and signal to noise ratio, the disk is resolved in thickness (Fig. 4).

### 3. Inner radial dust density

The flux observed in the mid-IR originates from the thermal emission of grains. Thus, in order to derive the dust density we need to know the grain temperature and emissivity. In the case

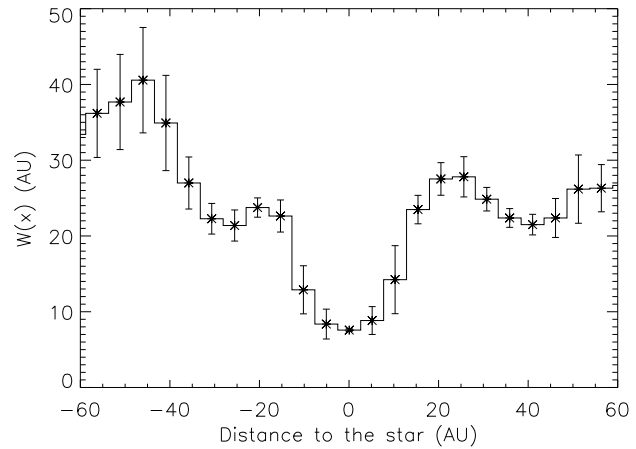


**Fig. 4.** The equivalent width (in AU) of the disk as a function of the distance  $x$  to the star (in AU). The thickness is defined as  $w(x) = \int_{disk} Flux(x, z) dz / \max(Flux(x, z))$ , where  $z$  is the direction perpendicular to the disk plane.

of a disk seen edge-on, as in the case with the  $\beta$  Pictoris system, an additional difficulty arises from the fact that the observed flux is integrated along the line of sight.

#### 3.1. Equations

Given the relatively small opening angle of the wedge disk (30 degrees), we can assume in first approximation that the dust temperature is constant in the direction perpendicular to the plane of the disk. The three-dimensional problem is then reduced to a two-dimensional problem. Under these conditions, the observed flux to be considered is the one-dimensional flux obtained by the integration of the signal in the direction perpendicular to the disk axis in the deconvolved image. The axes of the problem are defined as follows; the  $y$ -axis is parallel to the line of sight, and the  $x$ -axis is perpendicular to the line of sight. The radial surface density  $\sigma_i(r)$ , where  $i$  stands for N-E or S-W, is related to the observed flux profile,  $F_{obs}(x)$ , via the equation:

$$F_{obs}(x) = \frac{2}{d^2} \int_{x-\Delta x/2}^{x+\Delta x/2} \int_{r=x}^{\infty} \int_{sizes} \sigma_i(r) \pi a^2 Q_{abs}(a, \lambda) B_\lambda(T(r, a)) n(a) da \frac{r}{\sqrt{r^2 - x^2}} dr dx \quad (1)$$

where  $n(a)da$  is the number of grains having a radius between  $a$  and  $a + da$  and this distribution is normalized such that  $\int n(a)da = 1$ ;  $Q_{abs}(a)$  is the absorption coefficient of the grains and  $T(r, a)$  their temperature;  $B_\lambda$  is the Planck function at wavelength  $\lambda$  (i.e.  $12 \mu\text{m}$  for our mid-IR observations);  $d$  is the Earth- $\beta$  Pictoris distance,  $\Delta x$  is the spatial resolution of our image. Given the asymmetries found, we have considered the N-E and S-W sides separately. For each side, we have assumed invariance by rotation (see discussion in Sect. 3.5.2). For reasons of simplicity, we have also assumed, in a first step, that the grain properties are independent of the distance to the star.

In estimating IRAS fluxes, we have integrated the spectral energy density over each IRAS filter.

The temperature of the grains is calculated on the basis of energy conservation principle:

$$\left(\frac{R_\star}{r}\right)^2 \int_0^\infty Q_{abs}(a, \lambda) F_\lambda d\lambda = 4 \int_0^\infty Q_{abs}(a, \lambda) B_\lambda(T(a, r), \lambda) d\lambda \quad (2)$$

where  $F_\lambda$  is the star monochromatic emissive power of the A5V star  $\beta$  Pictoris and  $R_\star$  is the stellar radius of  $\beta$  Pictoris i.e.  $1.29 R_\odot$ .

In the case of grains containing ice, we have to take in account the heat used to vaporize ice and we use instead the equation (Lamy, 1974):

$$\left(\frac{R_\star}{r}\right)^2 \int_0^\infty Q_{abs}(a, \lambda) F_\lambda d\lambda = 4 \left[ \int_0^\infty Q_{abs}(a, \lambda) B_\lambda(T(a, r), \lambda) d\lambda + \frac{dE}{dt} L_s(T(a, r)) \right] \quad (3)$$

where  $\frac{dE}{dt}$  is the mass sublimation rate of the ice at temperature  $T$  and  $L_s$  is the latent heat of sublimation at the same temperature. As noted by Lamy, 74, we have found that this term is important only for temperatures higher than 150 K.

The dust properties (optical constants, size distribution) are key inputs to the model. We discuss hereafter how these inputs were determined.

### 3.2. Dust properties

#### 3.2.1. Composition and porosity

Key information about the nature of the dust in the inner part of the  $\beta$  Pictoris system arises from the observation of the characteristic silicate feature around 10 microns (Telesco et al., 1991; Knacke et al., 1993; Aitken et al., 1993). In LP94, following Knacke et al., 1993, we used Draine and Lee astronomical silicates (DL hereafter) as the constitutive material of the dust grains. However, when making a refined model of the disk, we can no longer use this kind of silicates. Indeed, they are not real silicates, but a "mixture" introduced to reproduce observations of the interstellar medium, whereas the spectrum observed in  $\beta$  Pictoris is more similar to that of comet Halley. If we examine carefully the spectrum, we can notice very sharp structures at 9.7 and 11.3  $\mu\text{m}$ , showing that the silicates must be partly crystalline (contrarily to DL silicates, which are only amorphous). However, the relatively broad feature around 10  $\mu\text{m}$  suggests that amorphous silicates represent a relatively important part of the grains composition. We may also use porous grains, as the grains of the solar system are sometimes porous (e.g. Greenberg and Hage, 1990 and references therein). The absorption coefficient of a mixture of different kinds of silicates (eventually porous) has been calculated according to the Maxwell-Garnett

effective medium theory (Bohren and Huffmann, 1983) combined with Mie theory, an approach that has been shown to be useful in deriving the absorption coefficients of porous particles (Hage and Greenberg 1990; Kozasa, Blum and Mukai, 1992). Additionally, we used the optical constants deduced from laboratory measurements (Dorschner et al., 1995, for amorphous olivines and pyroxenes; Mukai and Koike, 1990, for crystalline olivine).

Greenberg and Li, 1995, have put forward the hypothesis that the  $\beta$  Pictoris dust was created by evaporating comets. Thus, grain properties follow a model of cometary dust proposed by Greenberg and Hage (1990). In this model, they suggest that the comets, the most primitive bodies of the solar system, are made of unmodified protosolar nebula interstellar dust. This interstellar dust, according to the models developed by Greenberg, 1985, is mostly composed of particles with a silicate core and with an "organic refractory" mantle. While we do not describe in detail the optical properties of this material, we notice several interesting points:

- This mantle adds a feature in the spectrum around 8  $\mu\text{m}$ , leading to a better fit of the 10  $\mu\text{m}$  spectrum than in the case of silicate grains without a mantle.
- They have absorption coefficients that are relatively high in the optical range (albedo around 0.4). As a consequence, these particles have a higher temperature than the "naked" silicate grains which generally have an albedo around 0.8. Their high temperature is also partly due to the fact that these particles are very porous ( $P=0.984$ ). This makes these type of grains an interesting candidate to explain why we are able to detect in our images at 11.9  $\mu\text{m}$  the disk up to distances as far as 100 AU from the star. If the particles were relatively "cold", this would imply a large number of particles hardly compatible with the measured scattered flux at 100 AU.

Greenberg and Li claim they can obtain a better fit of the 10  $\mu\text{m}$  spectrum when using these type of grains instead of simple silicate grains. Thus we have also considered this type of grain in our models.

#### 3.2.2. Size distribution

There is limited information about the particle size distribution in  $\beta$  Pictoris. In the inner part of the disk, the only information comes from the presence of the silicate feature in the spectrum, which requires particles as small as a few  $\mu\text{m}$ . In the outer part of the disk ( $r > 100$  AU), the absence of significant colour excess in visible observations (Paresce and Burrows, 1987), implies that the dominant particles for the scattering are larger than a few  $\mu\text{m}$ .

From the theoretical point of view, we know that compact grains smaller than about 2  $\mu\text{m}$  are very efficiently expelled, by radiation pressure (Artymowicz, 1988). Larger grains are also removed from the system for instance by Poynting-Robertson effect or by collision. Besides, we can expect that processes like collisions and dust release by  $\beta$  Pictoris grazing comets may replenish the medium with small particles. The resulting size distribution is thus difficult to predict. In the following we

have taken a pragmatic approach, i.e. a power law for the size distribution (with two cut-off sizes, the maximal one being fixed in all the models to  $1000 \mu\text{m}$ ) where we allow a change in the power law index at a given size. It gives three free parameters that will be found when trying to fit the different observables of the disk ( $10 \mu\text{m}$  spectrum, IRAS fluxes, scattered fluxes).

### 3.3. Inversion algorithm

Eq. 1 is an ill-posed problem because of the additive noise in the data,  $F_{obs}(x)$ , and makes the Abel transform method inefficient (Craig, 1986). However, several techniques can be used to solve these kind of problems, whose most popular application is the image restoration. We chose the Maximum Entropy method (Gull and Skilling, 1984), but using the cross-entropy instead of absolute entropy to avoid about the problem of determining the value of the parameter "m" ("model" in Gull and Skilling algorithm). This parameter represents the value of the background in the absence of any object in the data (e.g. the background of an image). In our problem, there is no real background value, thus we prefer a method in which the amount of information is not calculated by comparison to a reference value (m), but in which the information provided by a data value is quantified by comparison to its nearby values. This method is very robust in the cases of noisy problems with lack of data, and has proved to be efficient in giving the simplest solution compatible with the data for a wide field of inverse problems. This procedure was applied for each side (NE and SW), assuming invariance of all quantities by rotation around the z-axis perpendicular to the disk plane.

The deduced surface density; using core-mantle silicate grains according to Greenberg et al. models; is shown in Fig. 5 and the normal optical thickness  $\tau$  is plotted in Fig. 6. Assuming a volumic mass of the grains of  $2.5 \text{ g cm}^{-3}$ , the total mass of dust is  $2.4 \times 10^{21} \text{ g}$  inside a radius of 10 AU, that is compatible with the total dust mass obtained previously in that region (Aitken et al., 1991; Backman et al. 1993; Knacke et al., 1993). The surface density again shows an inner void of matter.

### 3.4. Fit of the $10 \mu\text{m}$ spectrum

We constructed the disk spectrum inside a 4 arcsec beam deduced from the surface density found above and compared it to the spectrum obtained by Knacke et al. (1993). We have tested various compositions of the grains based on basic silicate materials (olivines, pyroxenes, crystalline olivine). Using this assumption, we were unable to fit correctly the  $10 \mu\text{m}$  spectrum of the disk measured by Knacke et al. when using any mixture of silicates or when varying the size distribution index. We only noticed (according to the remark of Knacke et al., 1993) that the fit was slightly better around  $8 \mu\text{m}$  when we used a mixture of olivine and pyroxene instead of pure olivine.

As said previously, Greenberg and Li proposed their model of core-mantle (mantle of refractory organics) silicate grains to reproduce the  $\beta$  Pictoris spectrum. We have also attempted to use this material. We found that we could obtain a good fit of the

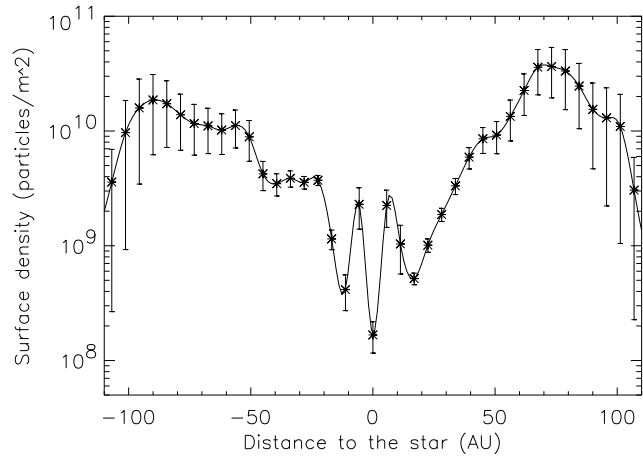


**Fig. 5.** The surface density of the inner  $\beta$  Pictoris dust disk deduced from our  $10 \mu\text{m}$  data. We have used core-mantle silicate particles following the Greenberg et al. models.

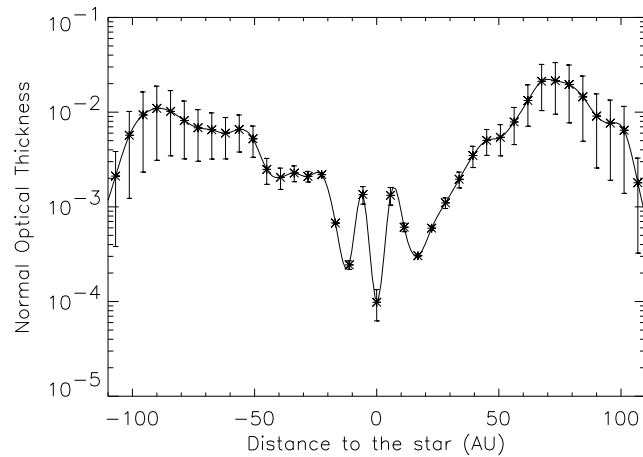


**Fig. 6.** The normal optical thickness of the disk (i.e.  $\tau(x) = \int \pi a^2 Q_{ext} \sigma(r) n(a) da$ ) that gives an indication on the number of particles independent from the size distribution.

$10 \mu\text{m}$  spectrum with this material ( $\chi^2 = 18$ , number of "free" parameters = 35), even better than the fit obtained by Greenberg and Li, because, contrary to them, we used the density of particles in the inner regions deduced from our observations (instead of taking a power law), and also because we took for the core silicate a mixture of pyroxene and olivine instead of olivine only (we took a mixture of 55% of amorphous olivine  $\text{MgFeSiO}_4$ , 35% of amorphous pyroxene  $\text{Mg}_{0.6}\text{Fe}_{0.4}\text{SiO}_3$ , and 10% of crystalline olivine: this composition is similar to the one found by Sanford, 1988, for interplanetary particles of our solar system). One builds a macro, porous grain ( $P=0.98$ ) from elementary  $0.1 \mu\text{m}$  sized particles (see Greenberg and Hage, 1990). For such an elementary grain, the mantle of organic refractories has a volume fraction twice that of the silicate component (or roughly equal in mass since the volumic mass of the refractory organics is the half that of the silicate one). The indexes of the

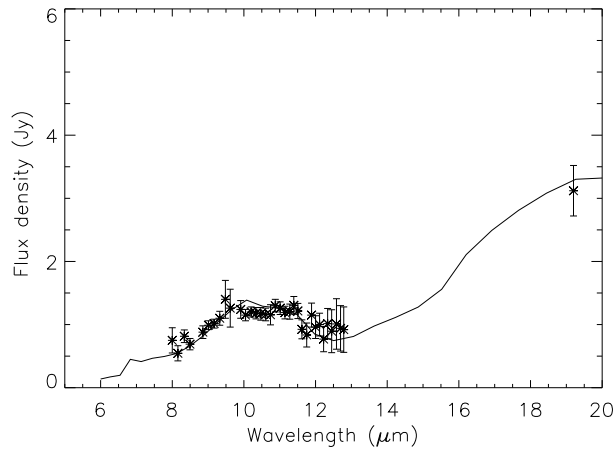


**Fig. 7.** The observed and reconstructed spectra of the inner  $\beta$  Pic dust disk (inside a 3.7 arcsec beam). Plain line: the reconstructed spectrum using core-mantle silicate grains, the stars represent the data of Knacke et al., 1993, combining IRTF and Big Mac data. The corresponding  $\chi^2$  is 18 (this must be compared to the number of measurement points; 35). We have normalized the spectra at 11.9  $\mu\text{m}$  since our density is deduced from an averaged flux over the 10.5–13.3  $\mu\text{m}$  filter.

size distribution were:  $-3.0$  from 0.1 to 10  $\mu\text{m}$  and  $-3.3$  from 10 to 1000  $\mu\text{m}$ . These values are not crucial for the fit of the 10  $\mu\text{m}$  spectrum but as we will show in the section concerning the fit of the IRAS data, the IRAS fluxes constrain strongly these values. It is also interesting to note here that this type of size distribution is very close to the estimated size distribution of the interplanetary particles in our solar system (cf Mukai, 1990). The spectrum obtained and the data of Knacke et al., 1993, are superimposed in Fig. 7.

It must also be noted that DL silicates give a relatively acceptable fit to the 10  $\mu\text{m}$  spectrum ( $\chi^2 = 30$  using an index of  $-4.0$  for all sizes from 0.1 to 1000  $\mu\text{m}$ , see Fig. 8) so we cannot rule them out as possible candidate even if, as explained above, we refrain to use them because their optical constants are not deduced from laboratory measurements.

### 3.5. Discussion

#### 3.5.1. Influence of the dust properties on the inner profile

To show that the result of an inner depleted region is robust if the assumptions on the sizes of the grains (composition, index of distribution and cut-off values) are changed, we have tested different size distributions by varying the index of the power-law within the range  $\{-2, -4\}$ ; changed the lower cut-off radius from 0.1  $\mu\text{m}$  to 1  $\mu\text{m}$ , and varied the composition of the grains i.e. taking Draine and Lee astronomical silicate grains, olivine porous grains or even blackbody grains instead of core-mantle silicate grains. In every case, the inner depleted region is still here, confirming strongly the results obtained in LP94.

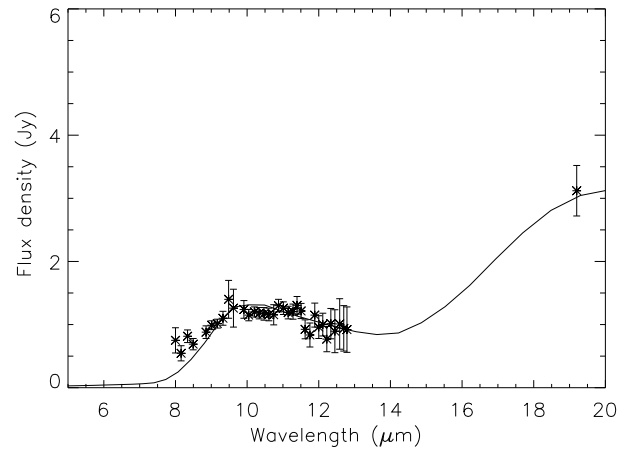


**Fig. 8.** Same as in Fig. 7, but using DL silicates grains, with a size distribution following a power-law with an index of  $-4.0$ , ranging from 0.1 to 1000  $\mu\text{m}$ . The corresponding  $\chi^2$  is 30.

#### 3.5.2. Invariance by rotation

In Eq. 1, we have assumed that the flux was radially axis-symmetrical on each side of the disk. However, we show here that this assumption is not crucial. Indeed when observing at 12  $\mu\text{m}$ , we are probing only a small part of the disk, located in an opening angle of about 30 degrees perpendicular to the line of sight if the density were radially constant, and a distorted cone when we modulate the cone using the “real” radial density (see Fig. 9 and its caption for the construction of the normalized map). This is due to the flux rapidly a fast decreasing with the distance (the flux is essentially fixed by the temperature of the grain). Then, the invariance by rotation assumed in the following section is likely to be verified in that region inside a 30 degrees angle.

#### 3.5.3. Scattering contribution at 12 microns

We have evaluated also the contribution of the scattered starlight at 12  $\mu\text{m}$ . The result show that it can be neglected within 100 AU, beyond which the scattered flux, varying as  $r^{-2}$ , supercedes over the thermal emission which varies much more rapidly with distance, because of the decreasing temperature of the grains. However, this contribution should be taken into account for observations with a more sensitive instrument like the ISO spacecraft, (we have even shown that the images made with the ISO-CAM 10  $\mu\text{m}$  camera should reveal scattered starlight beyond 150 AU).

#### 3.5.4. Comparison to Backman’s models

Backmann et al. (1993) have developed a series of models in order to reproduce their 10 and 20  $\mu\text{m}$  observations of the disk within two beams of 4 and 8 arcsec in diameter, and to fit the IRAS measurements. As shown in Fig. 10, their best model does not agree with our data.

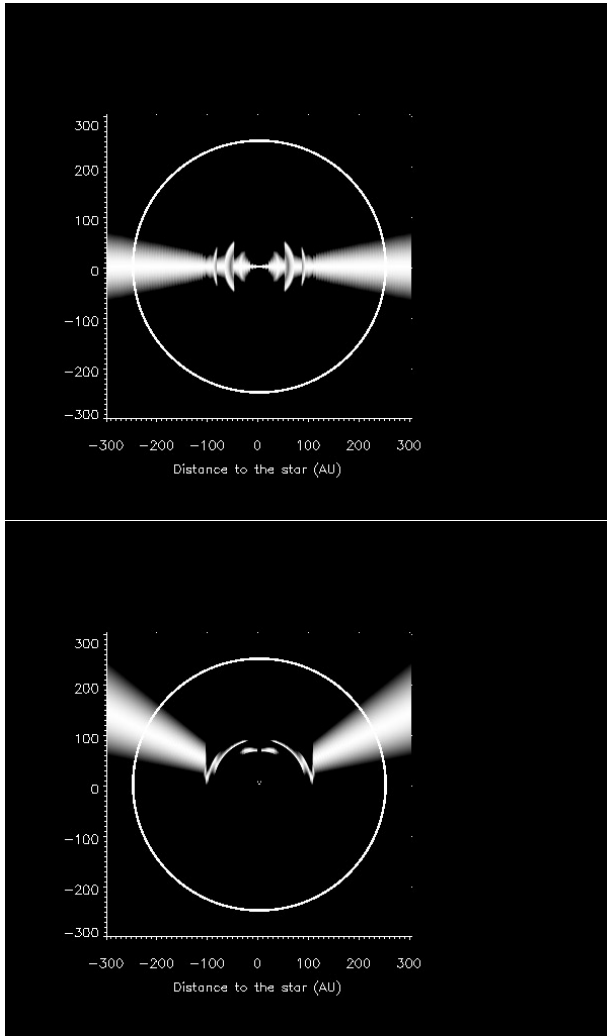


**Fig. 9a and b.** The 2D normalized maps showing the area where the thermal emission and the scattered light are emitted along a line of sight (the observer is assumed to be in  $y = +\infty$ , vertical axis). The normalization is such that at each point in  $x$ , the maximum emission is 1. Therefore, at a given  $x$  position, a “wide” emission corresponds to a local maximum in the density. We used the surface density plotted in Fig. 5. A bright ring has been overplotted in both maps to illustrate a 250 AU disk perimeter. Upper (a): thermal flux at 12  $\mu\text{m}$ ; lower (b): scattered flux in the R band showing the anisotropic effects of the scattering phase function. At each abscissae value, we have normalized the flux to a value of 1. The discontinuities in the maps are due to shape of the radial density; each time the density has a local maximum, the maps show a discontinuity.

However, it must be noted that they used crude absorption coefficients for the dust grains. Indeed, the coefficients were approximated by two power-laws as a function of the wavelength: an index of 0 (constant) for the lowest wavelengths ( $\lambda < \lambda_0$ ) and an index of -1 or -2 for the longer ones (where  $\lambda_0$  is a parameter depending on the size of the grains). If we carefully examine the real coefficients (see Fig. 11) we find out that for a fixed grain size (1  $\mu\text{m}$  in the case of Fig. 11), the shape of the

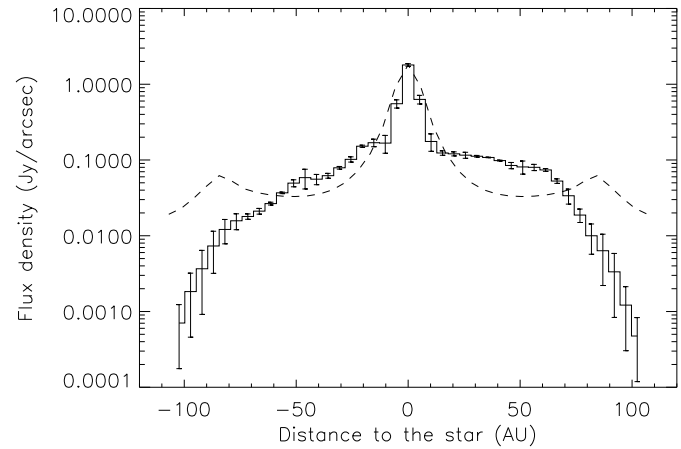


**Fig. 10.** The 12  $\mu\text{m}$  profile deduced from Backman's density in model 11 (dashed line), compared to profile deduced from our 10  $\mu\text{m}$  image of the  $\beta$  Pictoris disk (plain line).

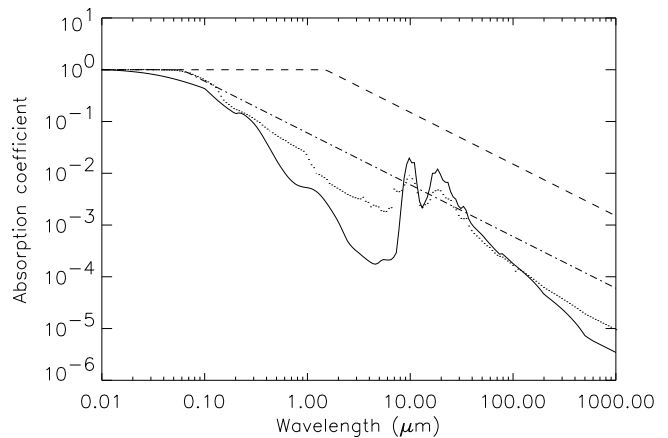


**Fig. 11.** The absorption coefficients of a grain of 1  $\mu\text{m}$  radius. We have plotted the absorption deduced from the Mie theory for porous olivine grains (plain line), and for core-mantle silicate porous grains (dotted line). For comparison, we have overplotted the approximated coefficients used by Backmann et al. in their models (1993): dashed line for a 1  $\mu\text{m}$  sized grain, dot-dashed line for a grain having a radius of 0.04  $\mu\text{m}$ . The high porosity of the grains we used in our models “shifts” the absorption coefficient towards smaller wavelength, corresponding to a smaller “effective” grain size.

real absorption curve with the wavelength is very different from the approximated one. Thus one must be critical of the results that use approximated absorption coefficients.

One key result of the Backmann et al. paper is the need of a two component model to be able to fit the IRAS fluxes. We have tried to check if such a conclusion remains valid when using less crude optical properties for the grains.

**Table 1.** Comparison with Backman’s measured photometrical fluxes at 10.1 and 20  $\mu\text{m}$ . CM stands for core-mantle silicate grains (size distribution: power law index of -3.0 from 0.1 to 10  $\mu\text{m}$  and -3.3 from 10 to 1000  $\mu\text{m}$ ). DL stands for Draine and Lee silicates with size distribution ranging from 0.1 to 1000  $\mu\text{m}$  and a power law index of -4.0.

Flux Source	beam diam.	$F_{10.1\mu\text{m}}$ (Jy)	$F_{20\mu\text{m}}$ (Jy)
Backmann	4''	$0.71 \pm 0.11$	$2.53 \pm 0.25$
Backmann	8''	$1.22 \pm 0.12$	$4.18 \pm 0.38$
Our density (CM)	4''	1.15	2.8
Our density (CM)	8''	1.8	7.4
Our density (DL)	4''	1.15	2.6
Our density (DL)	8''	1.6	6.4

## 4. Other observables

### 4.1. Outer density profile

Since we have no spectral signature of the dust in the outer regions, we have adopted, as a first attempt, the simplest solution, that is, no change change in the grain composition and no change in the size distribution between the inner ( $r < 100$  AU) and the outer regions. In order to be able to deduce the consequences of our derived density on other observables and check the compatibility with them (IRAS measurements, visible scattering profiles) we have had to extrapolate our density beyond 100 AU. The visible observations of the scattered starlight showed that the density should decrease for distances larger than 100 AU following a power-law with an index in the range [-1.5,-2.3] (Artymowicz et al., 1989; Kalas and Jewitt, 1995; Smith and Terrile, 1984). We have therefore extrapolated our density profile using a power-law density with an index of -1.7 index beyond 100 AU (Artymowicz et al. 1989).

### 4.2. Thermal emission

We tried to reproduce the photometric fluxes of the dust at 10.1 and 20  $\mu\text{m}$  measured by Backmann et al., 1993, with the IRTF, in 4 and 8 arcsec beams, including the effects of the convolution with the IRTF PSF. The results are given in Table 1.

The fluxes deduced from our surface density are in disagreement with Backmann et al. observations even taking into account the effects of the IRTF PSF. The Backman et al. data were taken at 3 air masses and used of the star  $\alpha$  Car as a calibrator. This leads to an underestimation of the measured flux in the Q band because the atmospheric transmission falls with increasing wavelength along the Q filter. In reality, the  $\beta$  Pic flux increases with wavelength (Backman, private communication). Secondly, the density grows rapidly with increasing distance to the star. It turns out that the 20  $\mu\text{m}$  flux is produced in a very large domain of distance to the star with two dominating regions: inside 10 AU and between 50 and 100 AU. As our data have large uncertainties in the last region, it may also explain the discrepancy with Backman et al. data.

We also tried to reproduce the fluxes in the IRAS bands of 12, 25, 60 and 100 microns. The results are reported in Table 2 where we indicate the predicted flux using the surface density deduced from our observations ( $r < 100$  AU) extended with a radial power-law with an index of -1.7 (Artymowicz et al. 1989; Backmann et al., 1993), and the total flux in a 100 arcsec beam measured by IRAS. The best results were obtained using DL silicates with an index of -3.5 for the size distribution but we have also list the fluxes given by our model that uses a smaller index more appropriate for fitting the 10  $\mu\text{m}$  spectrum (-4.0).

The results in Table 2 are in relatively poor agreement with IRAS fluxes except at 12  $\mu\text{m}$ , which is the wavelength at which density profile was deduced (all the 12  $\mu\text{m}$  comes the inner disk, i.e. inside 50 AU). This can be understood because, as explained in Sect.5, the 10  $\mu\text{m}$  data probes the dust in a narrow cone with an opening angle of about 30 degrees, while at longer wavelength the data are sensitive to much wider cones (the opening angle grows with wavelength). If there are azimuthal anisotropies in the density, the 25  $\mu\text{m}$  flux may not correspond to the density deduced from 12  $\mu\text{m}$  measurements. As seen in Table 2, the reproductibility of the IRAS fluxes depends dramatically on the chosen size distribution indexes. This means that the IRAS fluxes put the strongest constraints on the size distribution.

Finally, we have checked that our density and our dust mineralogy choice are consistent with sub-mm and mm observations. We found a flux of 97 mJy at 800  $\mu\text{m}$  compatible with Zuckerman and Becklin’s observations (1993) ( $115 \pm 30$  mJy), and 22 mJy at 1300  $\mu\text{m}$  (Chini et al, 1991 found  $24 \pm 2.6$  mJy) without assuming a size of the disk limited to 500 AU (since the disk has been traced as far as 800 AU from the star by Kalas and Jewitt, 1995).

### 4.3. Comparison with visible observations

As coronographic techniques improve with the use of adaptive optics, the limitations to observe the inner part of the disc will become less restrictive, and one should be soon able to observe the scattered starlight by dust particles in regions only accessible to infrared cameras up until now (Burrows et al., 1995, using the Hubble Space Telescope have succeeded very recently in observing the scattered light down to 20 AU). In order to assist these observations, we have constructed, using our surface density, a profile showing what one could see in the visible.

#### 4.3.1. Scattering models

As the Mie theory (to derive the scattering phase function) applies only to compact spherical grains (but it can be used to calculate the scattering coefficients in the case of porous grains, see Mukai et al., 1992), we used the different kinds of phase functions one can find in the literature. To modelize the scattering profile due to porous grains we used the Henyey-Greenstein phase function which is an approximation of the real phase function. It been used very often to fit the scattering properties of grains in various environments such as the interstellar medium (Mattila, 1970), planetary atmospheres (Irvine, 1975), and plan-

**Table 2.** Comparison between IRAS fluxes and one component models. Since the size distributions used to fit the  $10\ \mu\text{m}$  spectrum gave very poor fits, we have tried to modified the size distribution indexes, but the resulting model fluxes agree poorly with the IRAS measurements.

Flux Source	$F_{12\mu\text{m}}$ (Jy)	$F_{25\mu\text{m}}$ (Jy)	$F_{60\mu\text{m}}$ (Jy)	$F_{100\mu\text{m}}$ (Jy)
IRAS	$1.64 \pm 0.2$	$10.1 \pm 0.5$	$18.8 \pm 1.0$	$11.2 \pm 1.0$
Our dens. CM ind=-3.0/-3.3	1.75	10.42	4.5	1.37
Our dens. CM ind=-3.0	1.75	13.6	9.0	3.34
Our dens. DL ind=-4.0	1.67	9.02	4.9	1.3
Our dens. DL ind=-3.5	1.70	12.4	14.2	8.3

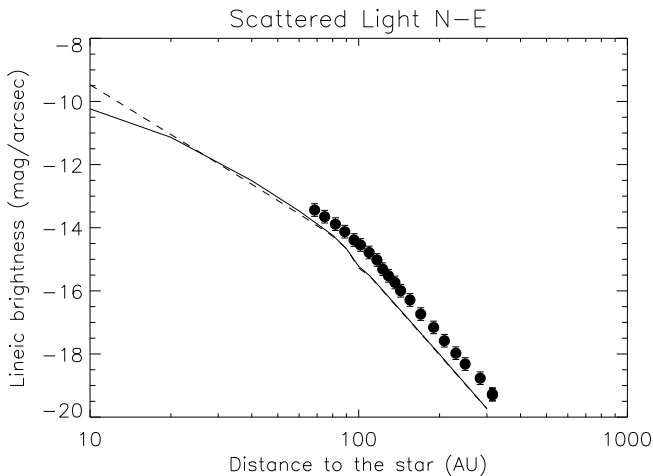


**Fig. 12.** The observed and reconstructed surface brightness profile of the N-E extension in  $\beta$  Pic using a one component model. Plain line: using Henyey-Greenstein phase function, dashed line: using Leinert empirical phase function (found in the Solar System). The stars are from the measurements of Kalas and Jewitt (1995).

etary rings (Cuzzi et al., 1984). We have also used the Leinert empirical phase function deduced from measurements of the zodiacal light in our solar system.

We have tried to reproduce the flux profiles in the R band measured by Kalas and Jewitt (1995). As shown in Figs. 12 and 13 the calculated scattered flux is slightly lower than the observed flux.

The observed scattered light at a given projected distance to the star are most sensitive to grains located further because (1) for the largest grains, the phase function is narrowly peaked in the forward scattering direction and (2) because the radial density peaks at 75 AU. If the disk is non-axisymmetric, observing the thermal radiation at  $12\ \mu\text{m}$  and the scattered light at  $0.6\ \mu\text{m}$  will not lead to the same density profile since they do not probe the same regions in the disk (see Fig. 9). This fact may explain the discrepancy about the S-W/N-E asymmetries which are very weak in visible, but can reach a factor of two in our data. For the same reasons, a discontinuity in the radial density will create a discontinuity in the derivative of the scattering profile at a distance somewhat closer to the star than the radial discontinuity. So if the break in scattered profile observed at 80 AU by many observers (Golimowsky et al., 1993; Kalas

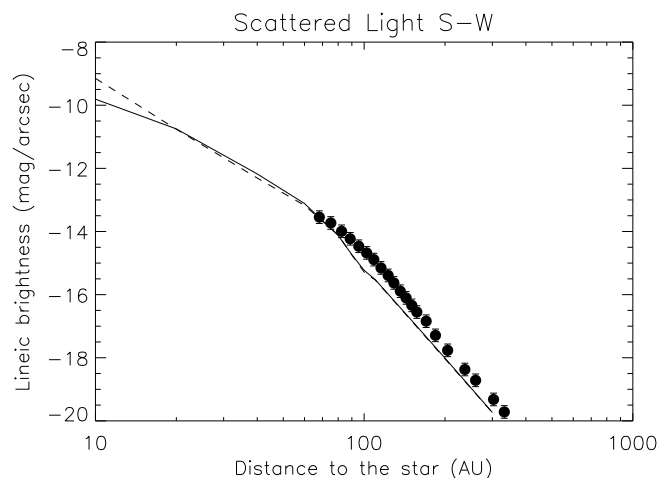


**Fig. 13.** Same as in Fig. 12 but for the S-W extension.

and Jewitt, 1995) is real, the corresponding radial discontinuity is located around 85-90 AU.

#### 4.4. Conclusion about the one component models

As shown above, one component the model allows only marginally to fit the IRAS data whose observed flux is, in majority, produced in the range [80-100 AU] where the density is maximum (it must be noted that it is also the case for all the longer wavelength, even for the 1.3 mm observations).

The results so far suggest that we should remove only one assumption, i.e. that the grains are composed of the same material everywhere in the disk.

## 5. Two component models

The temperature of the grains decreases continuously with increasing distance from the star. Within the disk of  $\beta$  Pictoris, water may exist in the form of vapor below the sublimation limit. When the temperature of the grains is low enough (below 110-120 K), any existing water vapor would condense preferably on the grains, thus creating icy particles. Alternatively, the grains could contain already some ice (e.g. fragmentation of comets) that sublimates if a large grain is broken into small pieces, which are hotter, or when the grains approaches the star. The optical properties of the grains containing ice are very different from

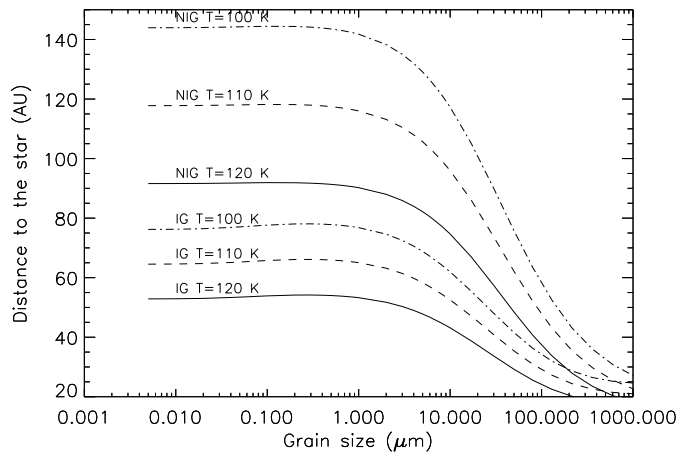


**Fig. 14.** A plot of the distances at which a dust grain reaches the temperatures of 100 K, 110 K, and 120 K, for two compositions: core-mantle silicate grains (NIG) and core-mantle silicate grains containing ice (IG) (14% of porosity replaced by ice, see below)

the properties of the non-icy grains. As a consequence, the temperatures of the grains are lowered (the iced grains absorb less of the visible emission of the star than pure olivine, and a part of the absorbed energy is converted into sublimation heat), and some characteristic ice features appear in the spectrum of the disk.

Having calculated the temperature of the iced grains as a function of from distance to the star, we found that the “ice boundary” for the small grains (i.e. smaller than  $10 \mu\text{m}$ ) where the temperature is between 100 and 120 K (for which the sublimation timescales are about 1 million years and 50 years respectively for a grain of radius  $1 \mu\text{m}$ , according to Backman and Paresce, 93), is located between 85 and 145 UA for non-icy grains, and between 55 and 80 UA for grains containing ice (see Fig. 14).

However, as suggested by Artymowicz, 1994, the efficient UV photospattering of the ice in the  $\beta$  Pictoris system may destroy the ice up to large distances from the star. Therefore, we have kept in our models the sublimation limit as a free parameter. In the models there is transition zone between 90 and 100 AU in which iced grains coexist with non-iced ones (the particles may be on eccentric orbits, or have a distance to the star that changes more rapidly than the sublimation/freezing timescales). In these models, the “naked” grains produce the  $10 \mu\text{m}$  flux that we detect up 100 AU, and the iced ones are responsible for the 60 and  $100 \mu\text{m}$  IRAS fluxes.

There are other elements in favor of the hypothesis of iced grains. Artymowicz et al., 1989, evaluated a model dependant upper bound to the albedo of the outer disk grains between 0.66 and 0.76 with a model independent lower bound of 0.5. Core-mantle silicate grains have an albedo around 0.4 which a bit low compared to the previous values, but if they are covered with ice, their albedo rises to a value of 0.65.

In the solar system the ice boundary is located at Jupiter’s orbit. The grains of Saturn’s rings are composed essentially of ice (Fink and Larson, 1975).

We took a power law of the iced component density (with an index between -1.7 (Artymowicz et al., 1989) and -2.5) connected (through a multiplicative scale factor, a free parameter in the range [1,10]) to the “hot” component at a distance from the star between 90 and 100 AU. The particle size distribution was assumed to be the same as the inner component. We used the same scheme as before to calculate the optical constants of the iced grains by using the Maxwell-Garnett mixing rule (we assumed that some part of the vacuum of the porous grains is filled by ice), and by calculating the absorption coefficients of the iced grains using the Mie theory. We tried then to fit the IRAS fluxes using the two component model, varying the percentage of ice in the grains, the ice boundary location and the step value. The size distribution could be slightly modified but we tried to keep it the same as in the inner regions.

The best fit was obtained with particles that are 14 % (in volume) ice, replacing some part of the vacuum (porosity). We have found that this value is constrained by the 100 to  $60 \mu\text{m}$  flux ratio. In this model, the “ice boundary” is located at a distance of 90 AU from the star. We used a “step” value of 1.8, and an outer component density decreasing like  $r^{-2.5}$ . In Table 3 we report the results obtained when trying to fit IRAS data. As mentioned before, the size distribution is strongly constrained by the IRAS fluxes (see Table 3), but the influence of the size distribution index on their fit is not as critical as in the one component model.

Looking at the Table 3, one notices that the two components model gives a very satisfactory fit of IRAS data when taking a size distribution ranging from  $0.1$  to  $10 \mu\text{m}$  with a power law index of -3.0 and -3.3 from 10 to  $1000 \mu\text{m}$  ( $\chi^2_{\text{IRAS}} = 2.7$ ).

The “step” value we have used in our models could in fact reflect a change in the sizes of the particles, or more simply an abrupt change in the number of particles, some of them (those composed of pure ice), for example disappearing because of sublimation.

### 5.1. Comparison to previous measurements in the visible

We checked that the two component model is compatible with visible coronagraphic observations. We again used the Henyey-Greenstein or Leinert phase functions for both the inner and outer components; however the grains in the outer component have a different porosity). The scattering profiles obtained are plotted in Figs. 15 and 16, with the coronagraphic data of Kalas and Jewitt (1995) superimposed. All the profiles appear to be compatible with their data.

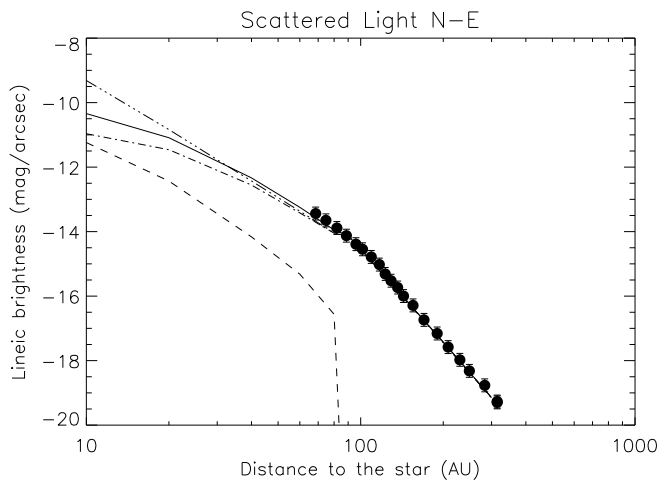
As seen in Fig. 9, the scattered light comes essentially from a half-ring located at a distance of 100 AU from the star. Looking at Figs. 15 and 16, we also notice that **the scattered flux coming from the outer component (grains with ice) is higher than the flux from the non-icy grains, down to a distance of 10 to 20 AU.**

**Table 3.** Comparison between IRAS Fluxes and the two component models (st= step used, ind. = index(es) of the size distribution).

Flux Source	$F_{12\mu m}$ (Jy)	$F_{25\mu m}$ (Jy)	$F_{60\mu m}$ (Jy)	$F_{100\mu m}$ (Jy)
IRAS	$1.64 \pm 0.1$	$10.1 \pm 0.5$	$18.8 \pm 1.0$	$11.2 \pm 1.0$
Our density ind=-3.0/-3.3 (st=1.8)	1.75	10.6	19.6	11.3
Our density ind=-3.0 (st=1)	1.73	13.4	21.0	12.4
Our density ind=-3.3 (st=2)	1.70	8.8	18.5	10.5

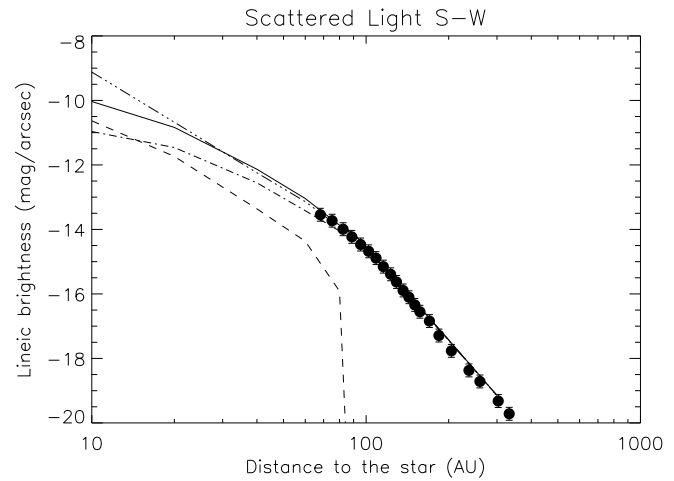
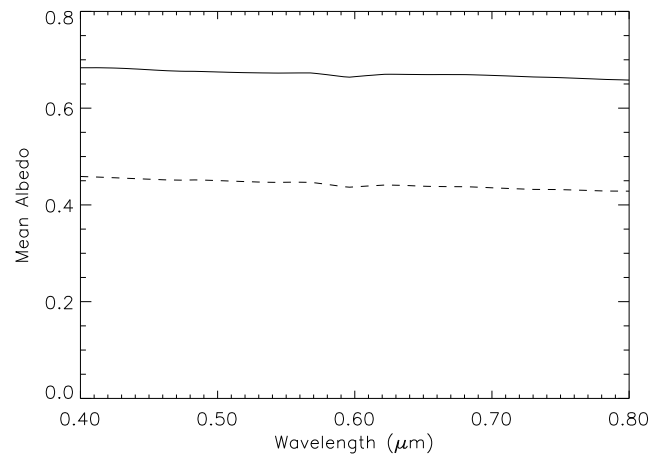
**Table 4.** Comparison with Backman's fluxes

Flux Source	Beam diam.	$F_{10.1\mu m}$ (Jy)	$F_{20\mu m}$ (Jy)
Backman	4''	$0.71 \pm 0.11$	$2.53 \pm 0.25$
Backman	8''	$1.22 \pm 0.12$	$4.18 \pm 0.38$
Our density (-3.0/-3.3)	4''	1.15	2.8
Our density (-3.0/-3.3)	8''	1.8	7.2
Our density (-3.0)	4''	1.15	3.1
Our density (-3.0)	8''	2.0	8.8

**Fig. 15.** The observed and reconstructed surface brightness of the N-E extension in  $\beta$  Pic. Dashed line: non-icy grains contribution to the scattered flux (Henyey-Greenstein phase function), Dot-dashed line: icy grains contribution to the scattered flux (Henyey-Greenstein phase function). Plain line represents the total scattered flux calculated using Henyey-Greenstein phase function. For comparison, we have also plotted (-.-.-) the total scattered flux using the empirical phase function of Leinert. The rounds are from the measurements of Kalas and Jewitt (1995).

This may also explain the fact that the scattered flux shows only small asymmetries (meanwhile the thermal flux shows asymmetries up to a factor of 2.3), even very close to the star (Lecavelier des Etangs et al., 1993).

Calculating the albedo of the outer material (iced grains) from the Mie theory, we have shown that it is roughly constant over the visible range, with a value slightly above 0.6 (see Fig. 17). This is consistent with the results of Paresce and

**Fig. 16.** Same as Fig. 15 but for the S-W extension.**Fig. 17.** Mean albedo (averaged over the size distribution) of the particles as a function of the wavelength. Plain line: outer component i.e. particles containing ice, dashed line: inner component

Burrows, 1987 who observed no significant color effects in the disk (within uncertainties of 20%), and the albedo estimated by Artymowicz et al., 1989 (a value between 0.66 and 0.76).

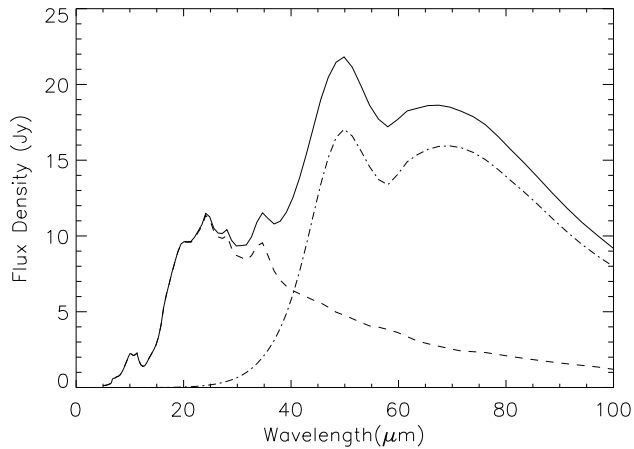


**Fig. 18.** Global spectrum of the  $\beta$  Pictoris disk deduced from the two component model. The dot-dashed line is the inner component contribution to the spectrum; the dashed line represents the outer (containing ice) density contribution.

## 6. Predictions

### 6.1. In the infrared

Now that we have a consistent model of the disk, we can make some predictions, in order to test the two component model we have presented.

First, the ice has some characteristic features at 3.1 and around 50  $\mu\text{m}$ . The feature at 50  $\mu\text{m}$  should be detectable by the ISO LWS and SWS). Fig. 18 shows an infrared spectrum covering the range 5-100  $\mu\text{m}$ . An wide emission feature very characteristic of ice can be seen, around 45-50  $\mu\text{m}$ . In the 10  $\mu\text{m}$  spectrum, the mantle of refractory organics creates an emission feature around 6-7  $\mu\text{m}$ . These features should be easily detectable in LWS and SWS spectra. Finally, we predict also that characteristic crystalline olivine features should be seen in the mid-infrared spectrum at 24, 28 and 35  $\mu\text{m}$ .

As noted before, the ISO infrared camera ISOCAM should essentially (in spatial extension) image the scattered starlight at 10  $\mu\text{m}$  when pointing at  $\beta$  Pictoris. It should also reveal a change in the particle composition characterized by a rapid decrease of the thermal emission (distributed on four 1.5 arcsec pixels of radius), replaced (but with an order of magnitude lower) by the scattered starlight.

In Fig. 19 we show a predictive 20  $\mu\text{m}$  profile, that should be compared to future 20  $\mu\text{m}$  imaging observations of the  $\beta$  Pictoris. At a wavelength of 20  $\mu\text{m}$  (by comparison to 10  $\mu\text{m}$ ), we are sensitive to colder (more distant from the star) dust, thus allowing to probe more accurately the disk in the range 50-100 AU. As shown in Fig. 19, the 20  $\mu\text{m}$  would confirm the change of composition at 85-100 AU by a very steep decrease of the flux in that region, because of a sudden jump in the temperature of the grains since iced grains are colder than core-mantle grains. These data should also resolve the discrepancy between our models and Backman et al. measurements at 20  $\mu\text{m}$  that we attribute to decreasing atmospheric transmission (which de-

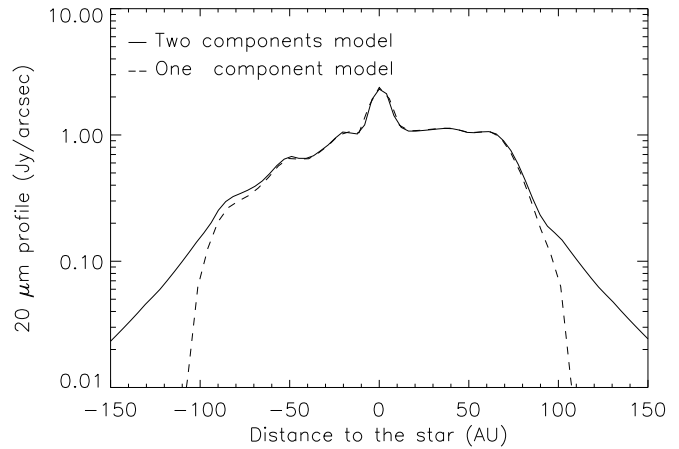


**Fig. 19.** The predicted profile of the  $\beta$  Pictoris dust disk at 20  $\mu\text{m}$ . The scattered flux has been taken in account but it is 3 orders of magnitude lower than the thermal flux at 100 AU and should be considered only for distances larger than 150 AU (but it is below the sensitivity limits from the ground).

pends critically on the weather) in the 20  $\mu\text{m}$  window leading to an underestimation of the flux.

### 6.2. In the visible

From the scattered flux we have deduced from our observations and our two components model, one notes that the scattered flux does not decrease when approaching the star. One must use a scattering model to compute the dust density and thus see clearly the inner gap in the dust. This can be understood from the superposition of two effects. First of all, the scattered flux is dominated by the iced outer component down to a very small distance from the star. Secondly, the flux received from the star decreases as  $r^{-2}$  ( $r$  being the distance to the star) a single dust grain, so, if the dust density increase in the central part of the disk (where the void is) is less fast than the decrease of that flux, one will observe a scattered flux slowly decreasing with  $r$ . Another significant effect is due to the scattering phase function: in all the physically realistic cases, the phase function shows an approximatively similar shape with a pronounced narrow maximum for scattering angles around zero. This means that the amount of scattered light, proportional to that phase function, increases rapidly for particles when they draw near the imaginary line joining the star and the observer and so they will dominate for small distances to the star. This increase can compensate a decrease of the particle density.

Thus, the simulations made using our density shows a scattered light profile that does not drop sharply when approaching the gap, but rather a fairly slow and continuous decrease.

We must be very cautious with the modeling of the scattered flux. At present, no rigorous way exists to reproduce theoretically the scattering due to porous particles, except using the Discrete Dipole Approximation (Draine, 1988) which requires a huge amount of computer resources to calculate the physical quantities (we are for the moment limited to a particle size of

about 1  $\mu\text{m}$ ). But with the everyday increasing power of the new computers, this should not remain a limit in the near future.

## 7. Conclusions

We have reported in this paper spatial observations we have made at 12  $\mu\text{m}$  of the  $\beta$  Pictoris dust disk. Our aim was to build a self consistent model of the disk, using constraints provided by our data and other observations available i.e. the IRAS measurements, the 10  $\mu\text{m}$  spectrum, the photometric measurements of Backman et al. at 10 and 20  $\mu\text{m}$ , the scattered flux in the visible range, and to a smaller extent, the sub-mm and mm fluxes. We first tried to make a model of the inner disk, i.e., inside a 100 AU radius, corresponding to the area we could probe with our 10  $\mu\text{m}$  images. We were guided by the 10  $\mu\text{m}$  spectrum of Knacke et al., 1993, to choose a composition of the grains, i.e. core-mantled silicate particles, following Greenberg and Li results, instead of the popular Draine and Lee interstellar silicates. In order to get the density, we had to invert the integral equation relating the observed spatial flux at 12  $\mu\text{m}$ , having first built a thermal model of the dust emission. The density shows an inner clearing zone in accordance with our previous results (LP94) and an asymmetry in favour of the South-West extension. This could be due to the effects of a planet on an eccentric orbit, sweeping out the dust and producing these asymmetries, but further simulations of the interaction between a planet and a dust disk have to be made to be able to give strong conclusions. In order to be able to check the coherence of our density with the other observables of the disk, we kept in a first attempt, the same composition of the grains and we extrapolated our density using a decreasing power-law in the outer disk ( $r > 100$  AU). We found that the compatibility with IRAS and 20  $\mu\text{m}$  data was only marginal, with a dramatic dependance of the fit to the size distribution index.

As it is likely that the coolest grains may be covered by an ice mantle, we constructed a second model in which the inner grains are covered with ice beyond the ice boundary (free parameter in our models). This time, the compatibility of our model with the observations was greater, with a lower dependance of the IRAS and 20  $\mu\text{m}$  predictions on the size distribution index, which makes us think that this model is much more accurate and physically acceptable than the single component model (in this model, ice is responsible for the high 60  $\mu\text{m}$  flux measured by IRAS). Furthermore, the two component model explains why we detect in our 10  $\mu\text{m}$  images a dust disk as far as 100 AU which implies a relatively high temperature of the grains (so they must have a low albedo in the visible and a low absorption in the far-infrared range), as opposed with an albedo around 0.7 in the outer disk, measured by Artymowicz et al., 1989. It reproduces also the break in the scattered flux at a distance around 100 AU, due to the iced component disappearing. It allows us to make some predictions concerning future observations of the disk i.e. for instance an infrared spectrum showing a intense peak of emission around 50  $\mu\text{m}$  produced by the ice mantles. We have also explained how to reconcile the questionss one could have about the strong asymmetries we see in the thermal flux, and

not detected in the scattered flux, showing that the thermal flux and the scattered visible flux do not probe the same regions in the disk.

However many question remain open:

- We have placed the location of the ice boundary at a distance of 90 AU, where the temperature of the grains is low enough to allow water condensation on the grains, however, some processes like the UV photosputtering may be efficient enough to push away the ice boundary up to larger distances from the star, or even destroy all the ice in the  $\beta$  Pictoris system.
- How to determine with precision the nature of the grains material and the size distribution. Since ground-based data are limited by the atmospheric spectral windows (N and Q bands), the spectra provided by the spectrographs SWS and LWS placed on the ISO spacecraft should be really helpful, especially to detect materials that give no characteristic spectral feature in the 10  $\mu\text{m}$  window (iron oxide for instance). The multiple crystalline silicate features in the range 15-80  $\mu\text{m}$  should give valuable informations on the the silicate sub-variety, i.e. the Mg/Fe (Magnesium to Iron) ratio in the olivine.
- How to interpret the fact that we detect a very pronounced asymmetry in the infrared and not in the optical range. We have tried to explain this in terms of different regions of the disk probed by the thermal imaging and the visible/near-infrared measurements (due to anisotropic phase function for the scattering). A partial answer may be brought about by 20  $\mu\text{m}$  imaging of the disk.
- To avoid questionable assumptions on the grain sizes, many other measurements need to be done at all available wavelengths, including polarization measurements (for instance polarization measurements in the infrared range may show a maximum correlated with the mean size). At the same time, a study of the grain dynamics could help to fix some physical limits on the sizes.

The two component model we have built to try to fit all the observables is probably not unique. We based our models on previous models of interstellar/cometary dust that recommend precise values of some parameters like the porosity or the amount of organic refractory relatively to the silicate material. These values may be different in the  $\beta$  Pic system. For instance some interplanetary particles are very porous (up to a porosity of 0.99) but others are not. The quick destruction of ice by UV sputtering remains an obstacle to the validity of models that include particles containing ice. We have considered uniform size distribution throughout the disk, but it is likely that it changes, since the collision rates vary with the distance to the star. The preliminary attempts we made to fit the observables with a single grain composition (core-mantle silicate) but a non-uniform size distribution failed, but we have not investigated all the possibilities.

## References

- Aitken, D. K., Moore, T. J. T., Roche, P. F., Smith, C. H. & Wright, C.M., 1993, *MNRAS*, 265, L41
- Artymowicz, P., 1994, *Circumstellar dust disks and planet formation*, R. Ferlet and A. Vidal-Madjar eds., Editions Frontieres
- Artymowicz, P., 1988, *ApJ*, 335, L79
- Artymowicz, P., Burrows, C. & Paresce, F., 1989, *ApJ*, 337, 494
- Aumann, H.H., 1985, *PASP* 97, 885
- Backman, D. E., Gillet, F. C., & Witteborn, F. C., 1992, *ApJ*, 385, 670
- Backman, D. E., Paresce, F., 1993, in *Protostars and Planets III* (eds Levy, E.H., Lumine, J.I. & Matthews, M.S.), Univ.Arizona Press, Tucson, 208
- Beust H., Lagrange-Henri, A. M., Vidal-Madjar, A., & Ferlet, R., 1990, *A&A*, 236, 202
- Burrows, C., et al., 1995, *AAS Bull.*, 187, #32.05.
- Campins, H., and Ryan, E., 1989, *ApJ*, 341, 1059
- Chini, R., Krügel, E., & Kreysa, E., 1990, *A&A*, 227, L5
- Craig, Ian J.D., 1986, in *Inverse problems in Astronomy: a guide to inversion strategies for remotely sensed data* (Adam Hilger Ltd eds.), 1986.
- Cuzzi, J.N., et al., 1984, in *Planetary rings* (Greenberg, R. and Brahic, A. eds.), Univ.Arizona Press, Tucson, 208
- Day, K.L., and Donn, B., 1978, *ApJ*, 222, L45
- Divine, N., et al., 1986, in *Space Sci.Rev.*, 43, 1
- Dorschner, J., Begemann, B., Henning, Th., Jäger, C., & Mutschke, H.N., 1986, *A&A*, 300, 503.
- Draine, B.T., 1985, *ApJS*, 57, 587
- Draine, B.T., 1988, *ApJ*, 333, 848
- Fink, U., & Larson, H.P., 1975 *Icarus*, 24, 411
- Ferlet, R., et al., 1993, *A&A*, 267, 137
- Golimowski, D.A., Durrance, S.T., & Clampin, M., 1993, *ApJL*, 411, L41
- Greenberg, J.M., & Hage, J.I., 1990, *ApJ*, 361, 260
- Greenberg, J.M., & Li, A., 1995, *The Role of the Dust in the Formation of Stars*, H.U. Käufel and R. Siebenmorgen eds., Springer: Berlin.
- Irvine, W.M., 1975, *Icarus*, 25, 175
- Kalas, P., and Jewitt, D. 1995, *AJ*, 110, 74
- Knacke, R. F., Fajardo-Acosta S. B., Telesco C. M., Hackwell J. A., Lynch D. K., & Russell, R. W., 1993, *ApJ*, 418, 440
- Koike, C. and Tsuchiyama, A., 1992, *MNRAS*, 255, 248
- Kosaza, T., Blum, J., & Mukai, T., 1992, *A&A*, 269, 423
- Lagage, P.O., Jouan, R., Masse, P., Mestreau, P., Tarrius, A. & Kauff, H., 1993, in *Infrared Detectors and Instrumentation*, (Fowler, A. W. eds.), Volume 1946, 655-666 (SPIE publisher)
- Lagage, P.O. & Pantin, E., 1994, *Nature* 369, 628
- Lagrange-Henri, A. M., Vidal-Madjar, A. & Ferlet, R., 1988, *A&A*, 190, 275
- Lamy, Ph. L., 1974, *A&A*, 35, 197
- Lecavelier des Etangs, A., et al., 1993, *A&A*, 274, 877
- Leinert, C., Link, H., & Pitz, E., 1993, *A&A*, 47, 221
- Lucy, L.B., 1974, *ApJ*, 79, 745
- Mattila, K., 1974, *A&A*, 9, 53.
- Mouillet, D., & Lagrange-Henry, A.M., 1995, in *The Role of the Dust in the Formation of Stars*, H.U. Käufel and R. Siebenmorgen eds., Springer: Berlin.
- Mukai, T., & Koike, C., 1990, *Icarus*, 87, 180
- Mukai, T., 1990, in *Evolution of interstellar dust and related topics*, A. Bonetti, J.M. Greenberg, S. Aiello eds., Elsevier Sci. Publ. Amsterdam, 397
- Mukai, T., Ishimoto, H., Kosaza, T., Blum, J., & Greenberg, J.M., 1992, *A&A*, 262, 315
- Okamoto, H., Mukai, T., & Kosaza, T., 1994, *Planet.Space.Sci*, 8, 643
- Richardson, B.H., 1972, *J. Opt. Soc. Am.*, 62, 55
- Roque, F., Scholl, H., Sicardy B. & Smith, B., 1994, *Icarus*, 108, 37
- Sanford, S.A., 1988, in *Dust in the universe*, (M.E. Bayley & D.A. Williams eds.), Cambridge: Cambridge University Press, 193
- Skilling, J., 1989, in *Maximum Entropy and Bayesian methods*, J. Skilling eds., Cambridge, England, 45
- Skilling, J., & Gull, S.F., 1984, *MNRAS*, 211, 111
- Skinner C.J., Barlow M.J. & Justtanont K. 1992, *MNRAS*, 255, 31p
- Smith, B. A., & Terrile, R. J., 1984, *Science* 226, 1421
- Starck, J.L., & Murtagh, F., 1994, *A&A* 288, 342
- Telesco, C.M., & Knacke, R.F., 1991, *ApJL*, 372, L29
- Telesco, C.M., Becklin, E.E., Wolstencroft, R.D., & Decher, R., 1988, *Nature*, 335, 51
- Vidal-Madjar, A., 1986, *A&A*, 167, 325